photonics

MDPI

Article

Random-Induced High-Contrast Subwavelength Nondiffracting Structured Light

Guangsen Guo [1,†], Junhui Jia [1,†], Xiaoshan Zhang [1], Junjie Chen [1], Shikuan Mai [1], Wenjia Wang [1], Haolin Lin [1], Yanwen Hu [1,2,*], Zhen Li [1,2,*] and Shenhe Fu [3]

[1] College of Physics & Optoelectronic Engineering, Jinan University, Guangzhou 510632, China; guogsen@stu.jnu.edu.cn (G.G.); jiajunhui@stu2020.jnu.edu.cn (J.J.); z237185@stu2023.jnu.edu.cn (X.Z.); 15813283281@163.com (J.C.); mskmsk@stu2023.jnu.edu.cn (S.M.); wangwenjia@stu2022.jnu.edu.cn (W.W.); linhaolin@jnu.edu.cn (H.L.)
[2] Guangdong Provincial Engineering Research Center of and Laser Technology, Guangzhou 510632, China
[3] Shandong Provincial Key Laboratory of Light Field Manipulation and Applications & School of Physics and Optoelectronics, Shandong Normal University, Jinan 250014, China; fushenhe@sdnu.edu.cn
* Correspondence: huyanwen@jnu.edu.cn (Y.H.); ailz268@126.com (Z.L.)
† These authors contributed equally to this work.

Abstract

Nondiffracting structured light has attracted considerable attention owing to broad applications in both the classical and quantum optics. Despite extensive research, existing generation approaches suffer from a contradiction between the subwavelength focal spot size and the strong side lobes, leading to a low-contrast localized light field in the far field. Here, we theoretically report a distinct technique for the generation of high-contrast nondiffracting structured light with its feature size reaching a subwavelength scale. The presented technique relies on a randomly perturbed sharp-edge aperture, which comprises a basic circular obstacle for exciting the in-phase high-spatial-frequency diffractive waves and randomized slit motifs for realizing destructive interference among the zero-order diffractive components, emerging from the sharp-edge diffraction. With this framework, we obtain a continuous high-contrast light needle, both for the zero-order light mode and the higher-order light with topological structure. In both cases, the resultant light fields preserve their subwavelength intensity profiles along propagation distance. This operating strategy provides an effective manner for structured light generation in the subwavelength scale, offering opportunities for advanced applications such as super-resolution imaging and nano-scale light–matter interaction.

Keywords: subwavelength nondiffracting structured light; random-sharp-edge diffraction

Check for updates

Received: 11 February 2026
Revised: 7 March 2026
Accepted: 11 March 2026
Published: 13 March 2026

Copyright: © 2026 by the authors. Licensee MDPI, Basel, Switzerland. This article is an open access article distributed under the terms and conditions of the Creative Commons Attribution (CC BY) license.

1. Introduction

Spatial diffraction and temporal dispersion are inherent properties of light waves, fundamentally leading to the spatial or temporal broadening of localized wave packets during propagation [1–3]. The diffraction- or dispersion-induced redistribution of light field from its on-axis region into surrounding areas considerably reduces the contrast between the central intensity peak and the background field, thereby limiting spatial and temporal resolution as well as the field of view in various optical systems [4,5]. Since the first experimental realization of the nondiffracting Bessel beam by Durnin et al. in 1987 [6,7]—generated through conical superposition of many plane wave components—considerable efforts have been devoted to overcoming the optical diffraction [8] and dispersion [9,10]. Particularly,

analytical solutions of the paraxial Helmholtz equation in different coordinate systems have given rise to several families of the nondiffracting light beams, including the Airy beams [11], Mathieu beams [12], and Weber beams [13]. These beams can self-accelerate in space, fundamentally different from the Bessel beam that propagates only along a straight line [6,7]. All the mentioned nondiffracting light beams exhibit self-healing property, namely they can restore their original wave forms during propagation even though they are partially blocked at their initial stage of propagation [14]. The concept of nondiffracting beams has been extended to other physical systems, leading to the generations of nondiffracting surface plasmon polariton waves [15] and acoustic waves [16] in space, as well as the nonspreading surface gravity water waves [17,18] and matter waves [19] in time. Owing to their distinctive features, nondiffracting wave packets have found wide applications in optical trapping [20], super-resolution imaging [21], plasma channel formation [22], and beyond.

Despite recent progress in this particular research field, most generated nondiffracting light beams exhibit transverse dimensions that are much larger than the optical wavelength. These relatively large-version nondiffracting light beams become uncompetitive in various optical nanotechnologies including nano-scale microscopy [23], nano-scale fabrication [24], and particle manipulation [25], as well as those associated with nano-scale light–matter interactions [26]. Therefore, the next challenge is to achieve the nondiffracting light beams at the subwavelength scale. Regarding this fundamental issue, it has been shown that one can exploit the surface plasmon polariton in the metallic system, which exhibits higher-spatial-frequency wave vector than the free-space one [27], allowing to produce much localized surface wave packet by interfering these higher-spatial-frequency components. Particularly, by appropriately arranging these high-spatial-frequency components on the metallic surface, one can generate the subwavelength nondiffracting beams [28,29]. However, these kinds of nondiffracting beams were realized in the (near-field) evanescent region, exponentially decaying along their propagation distance. To overcome this limitation, far-field approaches have been proposed and experimentally demonstrated. For example, metasurface with sharp-edge elements has been designed to excite propagating high-spatial-frequency waves [30] (different from the evanescent ones excited in the near field), giving rise to the generation of deep-subwavelength structured light in the far field [31,32]. In addition, some have considered utilizing the quantum superoscillatory phenomenon (a far-field quantum wave phenomenon of a band-limited wave function which locally oscillates at a frequency faster than its maximum Fourier component [33]) to realize the superoscillatory light fields with deep-subwavelength feature sizes [34,35]. These far-field superoscillatory light fields can be achieved and made nondiffracting during propagation in space, with particularly designed subwavelength structures [36,37] and diffractive optical elements [38,39]. Nevertheless, these far-field approaches often encounter a serious problem that the generated subwavelength main lobe of the light field is inevitably accompanied with strong sidelobes [32,40], thereby considerably reducing subwavelength light contrast, which limits its potential applications.

In this work, we propose and demonstrate a randomly perturbed sharp-edge aperture, capable of generating high-contrast nondiffracting light beams at the subwavelength scale. The proposed structure includes a basic circular disc with sharp edges, which is used to excite the propagating high-spatial-frequency wave vectors with cylindrically symmetric distribution in the Fourier space. The constructive interference between these in-phase high-spatial-frequency components results in a tightly confined nondiffracting light needle with feature size at the subwavelength scale. On the other hand, our designed sharp-edge structure comprises slit motifs, separately distributed in rotationally symmetric positions that are surrounding the basic circular disc. The slit width of these individual

motifs varies randomly, allowing us to realize the destructive interference between the zero-order diffractive components emerging from the sharp-edge diffraction of the structure, while maintaining the constructive interference of the high-spatial-frequency diffractive components along the on-axis positions. As a result, we are able to form a high-contrast nondiffracting light beam in the subwavelength-scale regime. The presented mechanism offers a robust and effective route toward the generation of the high-contrast subwavelength nondiffracting structured light, paving the way for future advanced applications such as in the optical super-resolution imagings, and nano-particle manipulations.

2. Working Principle

To realize the high-contrast subwavelength nondiffracting light beams, it is essential to achieve coherent superposition among these high-spatial-frequency diffractive components while randomizing the phase of the zero-order diffractive components in the course of sharp-edge diffraction. At the beginning, we consider a sharp-edge obstacle to excite these high-spatial-frequency diffractive components, which propagate to the far field. Specifically, we consider an incident optical wave, which is partially cut by the sharp-edge obstacle. At a local position near the sharp edge, the incident light field features an abrupt change when it hits the edge of the obstacle, described by a step function $f(x,y) = \mathrm{step}(x,y)$, where (x,y) represents the local position of the sharp edge. Such a step wave function leads to an abrupt phase change, which, due to prominent spatial phase gradient effect, produces abundant high-spatial-frequency diffractive components. From the view of the Fourier space, the Fourier transform of the step function indicates that the abrupt-change wave function exhibits a continuous higher-order diffractive components in addition to the zero-order one, all of which are able to propagate to the far field region. To ensure that these high-order diffractive components interfere constructively, their diffractive wave vectors must exhibit a cylindrically symmetric distribution in the reciprocal (Fourier) space. This requires a circular sharp-edge obstacle with its radius denoted as r_0. Thus, we realize abrupt phase change around the circle, generating the cylindrically symmetric diffractive wave vectors. Mathematically, the basic circular obstacle can be described as $C = 1 - \mathrm{circ}(r/r_0)$, where $r = (x^2 + y^2)^{1/2}$ and $\mathrm{circ}(\cdot)$ denotes a circle function, meaning that the function equals 1 if $r < r_0$ and 0 elsewhere. The geometric distribution of the sharp-edge obstacle is schematically depicted in Figure 1a.

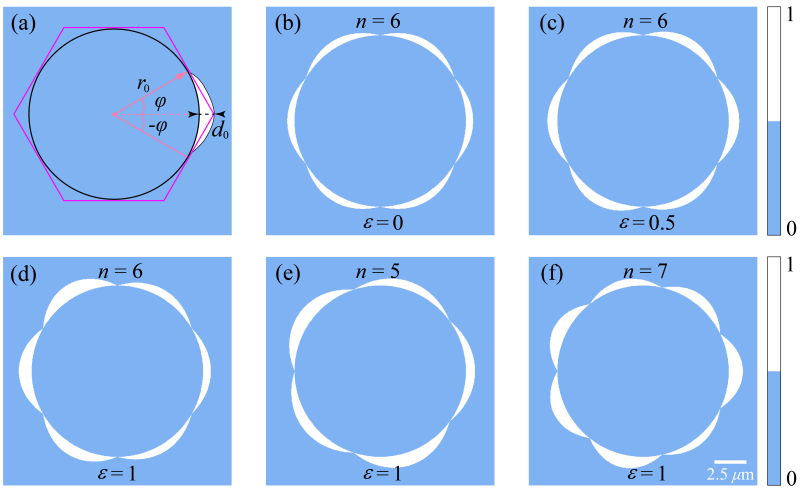


Figure 1. (**a**) Schematic illustration of the petal-like sharp-edge aperture. (**b**–**d**) The six-fold ($n = 6$) petal-shaped sharp-edge apertures with different degrees of structural randomness: (**b**) $\varepsilon = 0.0$; (**c**) $\varepsilon = 0.5$; (**d**) $\varepsilon = 1.0$. (**e**,**f**) Random-induced asymmetric petal-like sharp-edge apertures with pentagonal ($n = 5$) and heptagonal ($n = 7$) geometries. The randomness strength is set as $\varepsilon = 1.0$. These additional structures are used to verify the universality of our working principle.

In this circular sharp-edge configuration, not all the incident energy of light wave can be efficiently concentrated into the central (on-axis) spot by the circular obstacle through sharp-edge diffraction. Instead, a substantial portion of the energy is redistributed into the surrounding background through the interference of the zero-order diffractive components, namely the low-spatial-frequency components. This leads to a degraded focal contrast along the on-axis positions, as the intensity of the central main lobe is covered by the strong background field. To suppress these unwanted side lobes (the background light field), we modify the sharp-edge structure by including several sharp-edge slit motifs appropriately placed around the basic circular disc. This inclusion allows us to realize the destructive interference of these zero-order diffractive components while maintaining the constructive interference among the high-spatial-frequency diffractive components along the on-axis positions.

Specifically, the sharp-edge slit motifs (numbered as $k = 1, 2, \ldots, n$) are symmetrically distributed around the circular obstacle, with their angle locations expressed as $\theta_k = 2\pi(k-1)/n$. Figure 1a illustrates one of these slit motifs with its angle position located at $\theta_1 = 0$ with respect to horizontal direction; see the red dashed curve in Figure 1a. To disturb the phase of the zero-order diffractive components emerging from the basic circular obstacle, the spatial width of the individual slit motifs should be spatially varying. To achieve this purpose, we assume that the width of the individual slit motifs is dependent on the azimuthal angle θ, defined as $\theta = \arctan(y/x)$. In this case, we describe the width of the slit motifs as

$$\Delta r(\theta) = d_0 \cos\left[\frac{\pi}{2\varphi}(\theta - \theta_k)\right] \tag{1}$$

where d_0 represents the maximum width of the slit motifs and φ denotes an angle range that the slit motif covers, as displayed in Figure 1a. It is expressed as $\varphi = \pi/n$, determined by the number of the slit motifs (or the rotationally symmetric order). Thus, the angle θ varies between $-\varphi$ and φ. In this case, we obtain the following relation: $|\theta - \theta_k| \leq \varphi$, in each case of the slit motif. This setting indicates that the introduced slit motif connects the vertices of the n-fold regular polygon circumscribed around the inner disc, as shown in Figure 1a. Equation (1) shows that the width of the sharp-edge slit grows gradually with an increase of θ and then reaches its maximum value of d_0 and finally decreases gradually with θ. We emphasize here that the annular region between r_0 and $r_0 + \Delta r(\theta)$ is completely transparent, while the outer region remains opaque. Such abrupt changes of amplitude and phase of the incident light field allow to generate abundant high-spatial-frequency components that propagate to the far field region. Using such a designed principle, we obtain the complete sharp-edge slit motifs symmetrically surrounding the circle. As an illustration, Figure 1b depicts a 6-fold slit-motif pattern ($k = 1, 2, \ldots, 6$). It is evident that these slit motifs exhibit identical structural parameters and rotationally symmetric distribution in the transverse plane.

We note that such a slit-motif pattern is insufficient to obtain the high-contrast subwavelength focal spot, since, to some extent, these regular slit motifs (they exhibit periodicity along the azimuthal angle θ) still produce constructive interference among the zero-order diffractive components. In the following, we further disturb these in-phase interference effects by randomizing these slit motifs. To this end, we carefully break the structural symmetry in the azimuthal direction by introducing a random slit width. To achieve this, the maximum slit width d_0 in the individual slit motifs (see Equation (1)) is replaced by the following one:

$$d_k = d_0[1 + \varepsilon \cdot \mathrm{rand}(\cdot)] \tag{2}$$

where rand$(\cdot)$ denotes a uniformly distributed random variable with value ranging between 0 and 1 and ε controls the strength of the randomness. When $\varepsilon = 0$, the sharp-edge structure reduces to a perfectly regular slit-motif pattern, as illustrated in Figure 1b, while a larger value of ε (e.g., 0.5 and 1) introduces increasing strength of structural disorder; see Figure 1c,d for the case of the 6-fold slit motifs, respectively. We expect that this unique controllable symmetry-breaking pattern allows us to effectively suppress the interference effect of the low-spatial-frequency diffractive components and considerably enhance the contrast of the focal light spot along the on-axis positions.

Within these settings, the overall transmittance function of the randomly perturbed slit-motif aperture can be therefore expressed in polar coordinates as

$$T(r,\theta) = \begin{cases} 1, & r_0 \le r \le r_0 + \Delta r(\theta), \\ 0, & \text{otherwise}, \end{cases} \tag{3}$$

Note that here $\Delta r(\theta)$ incorporates the random modulation as mentioned above. Equation (3) represents an annular-like transparent region, determined by the inner radius r_0 and the randomly modulated outer radius $r_0 + \Delta r(\theta)$, thus forming a petal-like sharp-edge aperture. Using this design technique, we are able to obtain other slit-motif apertures having different rotationally symmetric distributions. Figure 1e,f depict the designed patterns having the five- and seven-fold rotationally symmetric orders, corresponding to the pentagonal and heptagonal configurations. In both these cases, the randomness strength is set as $\varepsilon = 1$.

When a monochromatic optical wave of carrier wavelength denoted as λ propagates along the $+z$ direction and illuminates the sharp-edge aperture located at $z = 0$ plane, the incident light field is modulated by the slit-motif pattern. The transmitted light field immediately behind the aperture structure can thus be written as a product of the incident light field $E_{\text{in}}(x,y)$ and the transmittance function $T(x,y)$ of the sharp-edge structure, namely $E_0(x,y,0) = E_{\text{in}}(x,y) \times T(x,y)$. The diffracted light field at a propagation distance $z > 0$ can then be calculated using the Fresnel diffraction integral, which can be expressed as

$$E(r,\theta,z) = \frac{\exp(ik_0 z)}{i\lambda z} \int_0^{2\pi} d\theta' \int_0^{r_0+\Delta r} E_0(x',y',0) \exp\left[\frac{ik_0}{2z}\left(r^2 + r'^2 - 2rr'\cos(\theta-\theta')\right)\right] r'\, dr' \tag{4}$$

where $k_0 = 2\pi/\lambda$ represents the free-space wavenumber. With this framework, we expect to observe the sharp-edge diffraction phenomenon and the resultant abundant high-spatial-frequency diffractive components in the reciprocal space, which are the basis to form the subwavelength light field in the far field. Particularly, the basic circular sharp-edge aperture generates the high-spatial-frequency diffractive components that constructively interfere along the optical axis, generating the focal spot analogous to the Poisson-Arago spot [41]. Owing to the superposition of these high-spatial-frequency waves, the obtained focal-spot size is expected to be in the subwavelength scale. On the other hand, the introduced randomly perturbed slit motifs play a complementary role to eliminate the wave effects from the zero-order diffractive components. As a result, we expect to realize the destructive interference at the off-axis region, considerably enhancing the contrast of the subwavelength on-axis main lobe.

3. Results and Discussion

To verify the working principle, we numerically investigate propagation dynamics of the light field behind the petal-like sharp-edge aperture, based on Equation (4). To demonstrate this, the incident light is assumed to be a plane wave with a wavelength of λ= 632.8 nm. In this case, the light field behind the aperture is reduced to

$E_0(x,y,0) = T(x,y)$, since $E_{\text{in}} = 1$ (in a normalized form). The incident plane-wave condition simplifies the numerical calculations. The simulation parameters are set as follows: radius of the basic circular disc $r_0 = 7.5$ μm, number of the slit motifs $n = 6$, and the maximum slit width $d_0 = 0.632$ μm. At the beginning, we study the scenario where the circular obstacle is not modulated by the slit motifs, with results depicted in Figure 2a,e,i. Figure 2a showcases the propagation dynamics, manifested by its intensity distribution in the x-z plane, whereas Figure 2e depicts its transverse intensity distribution at a propagation distance of $z = 9$ μm. These simulations indicate that a subwavelength light needle (nondiffracting light beam) with its full width at half maximum (FWHM) measured as 273 nm (indicated in the intensity profile in Figure 2i) is successfully achieved. This suggests that the resultant high-spatial-frequency wave vectors distribute in phase in the reciprocal space. However, this single circular sharp-edge aperture produces a strong background field originating from the zero-order diffraction that severely limits the effective field of view (see Figure 2e). To quantify efficiency of the generated subwavelength main lobe, we define a ratio between the peak intensities of the on-axis main lobe (I_m) and the strongest off-axis side lobe (I_s), written as $\eta = I_m / I_s$. This quantified expression shows that, if $\eta < 1$, the off-axis background field (side lobes) becomes dominant; if $\eta > 1$, the on-axis subwavelength light field becomes dominant. With this definition, we measure the ratio for the studied case depicted in Figure 2a,e,i as $\eta = 0.65$, suggesting a dominant background field in the far field.

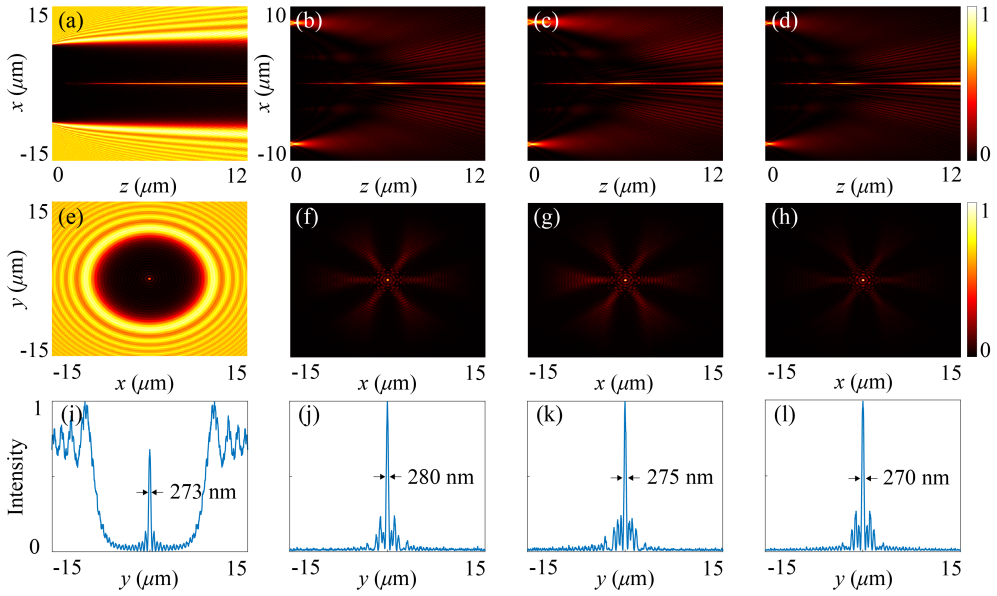


Figure 2. Numerical simulations for the subwavelength diffraction-free beams generated by differently designed sharp-edge apertures. (**a**,**e**,**i**) The recorded results obtained by a single circular obstacle: (**a**) Intensity distribution in the x-z plane; (**e**) Intensity distribution in the transverse plane, at $z = 9$ μm; (**i**) Intensity profile along y axis at $x = 0$. It is also measured at $z = 9$ μm. (**b**–**d**) Intensity distributions in the x-z plane, obtained by the six-fold slit-motif aperture, with different randomness strengths: (**b**) $\varepsilon = 0.3$; (**c**) $\varepsilon = 0.5$; (**d**) $\varepsilon = 1.0$. (**f**–**h**) The corresponding transverse intensity distributions in the x-y plane, recorded at $z = 9$ μm. (**j**–**l**) The corresponding one-dimensional intensity profiles along the y-axis at $x = 0$, which are extracted from (**f**–**h**). The FWHM values are measured as 280 nm, 275 nm, and 270 nm, respectively, comparable to the FWHM width in panel (**i**).

Then we study how the introduced random slit motifs influence the background field. The three columns on the right-hand side of Figure 2 display the diffractive behaviors of light wave after it passes through the randomized slit-motif apertures, with three different randomness strengths $\varepsilon = 0.3$, 0.5, and 1.0, corresponding to the results in Figure 2b,

Figure 2c, and Figure 2d, respectively. These three panels depict the intensity distributions in the x-z plane, revealing a continuous light needle along the on-axis positions. Compared to the result in Figure 2a, the randomly perturbed slit motifs are able to substantially reduce the background light field, as can be judged from their transverse intensity distributions in Figure 2f, Figure 2g and Figure 2h, respectively. Such a suppressed background light field is caused by the destructive interference of the zero-order diffractive waves. Specifically, the randomly modulated sharp-edge structure considerably reduces the phase coherence of the low-spatial-frequency components while maintaining the in-phase distribution of the high-spatial-frequency wave vectors in the reciprocal space. As a consequence, we observe a subwavelength light field located at the on-axis positions, propagating along the z direction without significant broadening. As for the slight oscillation of light intensity with propagation distance, it is caused by random pattern of the sharp-edge structure breaking the cylindrically symmetric distribution of the high-spatial-frequency wavevectors. The generated subwavelength nondiffracting light field exhibits high contrast, manifested by a high value of the generation efficiency η, measured as $\eta = 1.59, 1.67, 1.89$, respectively. Interestingly, as the randomness strength increases, the value of η shows a weak upward trend. Of course, from an energy perspective, most of the incident energy is blocked, resulting in lower energy in the focal region. In this regard, we believe that increasing the transmitting duty cycle of sharp-edge structure and altering the transmittance of the blocked area could potentially improve the energy efficiency. Moreover, to characterize the subwavelength feature size of the on-axis focal spot, we plot the one-dimensional intensity profiles of the light fields at the distance of $z = 9$ μm, along the y coordinate at $x = 0$, with results shown in Figure 2j–l, corresponding to the three different randomness strengths. The FWHM values of the main lobe are measured as 280 nm, 275 nm, and 270 nm, respectively, all below the diffraction limit ($\sim \lambda/2$). Using this designed technique, we are able to break the tradeoff between the central subwavelength light spot and the off-axis background field. Here, we not only eliminate the background field by means of the randomized slit-motif structure but also generate the nondiffracting light beam with feature size comparable to that shown in Figure 2i.

To further verify the robustness of the proposed slit-motif sharp-edge aperture, we perform different independent simulations with the randomness strength of $\varepsilon = 1$ while keeping other parameters unchanged. Figure 3 illustrates the simulated results for three different cases of random slit motifs. In these three random sharp-edge apertures, the maximum slit widths (in μm) of the individual slit motifs are randomly obtained as d_k = [0.8732, 1.0405, 0.7348, 0.7734, 1.2383, 0.9794], [1.2075, 0.9984, 0.9563, 0.7837, 0.9412, 0.8783], and [1.2363, 0.6417, 0.9170, 0.7480, 1.1222, 0.9548], respectively (here $k = 1, 2, \ldots, 6$). As shown in Figure 3a–c, all these three randomized configurations consistently produce the subwavelength nondiffracting Bessel-like beams along the on-axis positions, with weak side lobes accompanied. The overall beam morphology and intensity distribution near the on-axis region remain nearly identical, indicating that the subwavelength confinement of the light field is insensitive to the specific form of the random perturbations. Meanwhile, the background field is effectively suppressed in all these cases, due to the random-induced destructive interference effect among the zero-order diffractive components. At a propagation distance of $z = 9$ μm, quantitative analysis of the transverse intensity profiles (see Figure 3d–f) yields FWHM values of 289 nm, 271 nm, and 272 nm for the three representative configurations, all well below the diffraction limit. In addition, we also calculate the spot size (FWHM value) for different propagation distances. For example, in the case of $n = 6$ and $\varepsilon = 1$, the calculated results are shown in Figure 4a. It can indeed be seen that the focused spot sizes are all at the subwavelength scale, and there is no obvious broadening. The robustness of these diffractive behaviors can be understood as follows:

The circular sharp edge (the basic obstacle) in all these randomly modulated structures coherently excites the high-spatial-frequency diffractive components with their wave vector distributed in phase, leading to constructive interference along the optical axis. By contrast, the randomized slit motifs (regardless of the structure involved) introduce phase perturbations among the low-spatial-frequency diffractive components, which gives rise to destructive interference effect in the off-axis region.

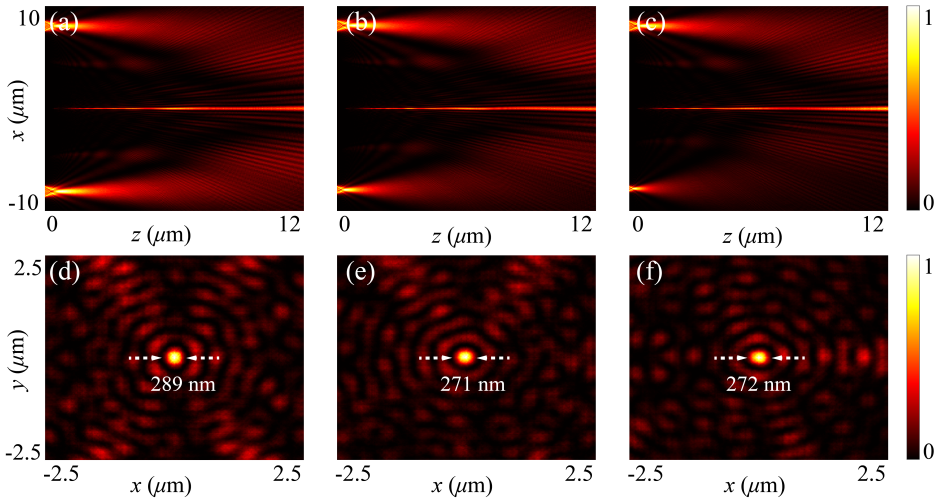


Figure 3. Subwavelength generation of the nondiffracting beam using six-fold ($n = 6$) slit-motif aperture with three different randomized structures. In all these cases, the randomness strength is set as $\varepsilon = 1$. (**a**–**c**) The recorded intensity distributions in the x-z plane for three different cases of randomized structures. (**d**–**f**) The corresponding transverse intensity distributions to (**a**–**c**), recorded at the propagation distance of $z = 9$ μm. The corresponding FWHMs are measured as 289 nm, 271 nm, and 272 nm, respectively.

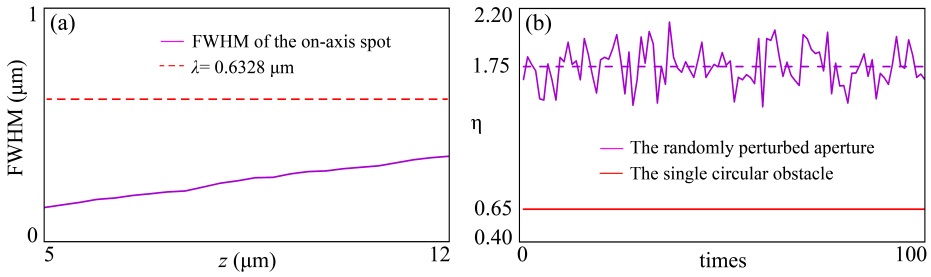


Figure 4. (**a**) The FWHM values of focused spot corresponding to different propagation distances after passing through the random structure (purple curve). The red dashed line for comparison indicates the wavelength value used. (**b**) Subwavelength generation efficiency for the randomly modulated aperture of $n = 6$ and $\varepsilon = 1$ (purple curve) and the single circular obstacle without random modulation (red curve).

Figure 4b further quantifies the high-contrast subwavelength light field. For comparison, the red curve depicts the generation efficiency of the subwavelength light field obtained by the sharp-edge circular disc (without random modulation), showing a much lower efficiency due to the pronounced sidelobes (the background light field). By contrast, statistical analysis over 100 independently simulations for the randomized apertures ($n = 6$, $\varepsilon = 1$) shows that the focusing efficiency remains much higher than 1, indicating the generated high-contrast subwavelength main lobe. Due to the random effect, we observe that the efficiency curve exhibits slight fluctuation around an average value of $\eta = 1.75$. The efficiency curve obtained by the 100-time simulation confirms that the random-induced destructive interference among the low-spatial-frequency diffractive components is ro-

bust and reproducible, suggesting a novel mechanism for achieving the high-contrast subwavelength nondiffracting light beam.

To confirm the universality of the proposed mechanism, we investigate the focusing performance of the randomized petal-like apertures with different numbers of the slit motifs, where the geometric symmetry is intentionally broken in the azimuthal direction. The random perturbation with randomness strength set as $\varepsilon = 1$ is applied to the pentagonal ($n = 5$) and heptagonal ($n = 7$) slit-motif apertures, as illustrated in Figure 1e and Figure 1f, respectively. Owing to the reduced rotational symmetry, both the sharp-edge configurations generate well-defined subwavelength nondiffracting light beams with high contrast, measured as $\eta = 1.71$ and $\eta = 1.70$; see Figure 5a–c and Figure 5d–f for the two configurations, respectively. Figure 5a,d illustrate that the resultant light beams remain highly stable, exhibiting nearly nondiffracting propagation along distance. As shown in Figure 5b,e the broken symmetry of the slit-motif sharp-edge aperture causes only slight distortions in the off-axis intensity profiles, while the central bright core remains tightly confined, preserving its intensity profile along the propagation distance. Quantitative analysis reveals the FWHM values of 281 nm and 273 nm for the pentagonal and heptagonal cases, respectively, as indicated in their intensity profiles in Figure 5c,f. Consequently, the proposed working principle exhibits strong tolerance to both the structural randomness and the number of the slit motifs.

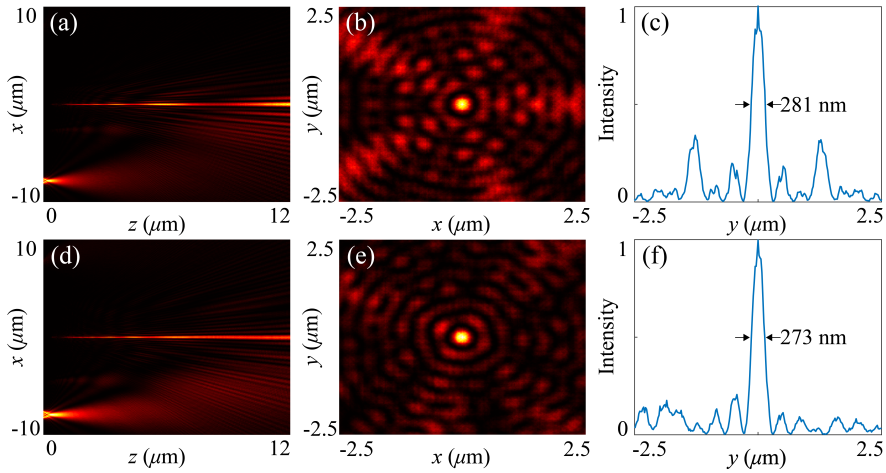


Figure 5. Generation of the subwavelength nondiffracting light beams using petal-like sharp-edge apertures with different rotationally symmetric orders: (**a**–**c**) The symmetric order is $n = 5$, corresponding to the pentagonal aperture; (**d**–**f**) The symmetric order is $n = 7$, corresponding to the heptagonal aperture. (**a**,**d**) The recorded intensity distributions in the x-z plane. (**b**,**e**) Intensity distributions in the transverse plane, recorded at the propagation distance of $z = 9$ μm. (**c**,**f**) One-dimensional intensity profiles corresponding to (**b**,**e**), revealing subwavelength focal spots with FWHMs of 281 nm and 273 nm, respectively. The randomness strength is set as $\varepsilon = 1$.

Finally, we examine the propagation dynamics of a vortex light beam when it is diffracted by the randomly modulated slit-motif aperture. In this case, we modify the incident light field as $E_{\text{in}}(x, y) = r/w_0 \exp(-r^2/w_0^2) \exp(im\theta)$, where w_0 denotes the initial width of the vortex light beam and m represents the topological charge. It is no longer an incident plane wave but a structured light beam with helical wavefront and a hollow beam profile described by the Laguerre–Gaussian (LG) function. For simplicity, here we study the case of $m = 1$. Hence, the initial condition therefore becomes $E_0(x, y, 0) = r/w_0 \exp(-r^2/w_0^2) \exp(i\theta) \cdot T(x, y)$. In the simulation, we consider the six-fold slit-motif aperture (as shown in Figure 1d) as illustrations, with randomness strength set as $\varepsilon = 1.0$, while keeping other structural parameters unchanged. The width of the LG profile is chosen as $w_0 = 10$ μm. With these settings, we obtain the results,

as depicted in Figure 6. As a reference, we first investigate the sharp-edge diffraction by the single circular obstacle, with results shown in Figure 6a–c, demonstrating the intensity distribution in the x-z plane, transverse phase distribution at $z = 9$ μm, and the one-dimensional intensity profile at $z = 9$ μm, respectively. It is evident that a subwavelength nondiffracting vortex light beam can be generated in the far field. The subwavelength feature size is characterized by its peak-to-peak distance of the on-axis vortex field, as indicated as 448 nm in Figure 6c. It means that the designed sharp-edge aperture is able to recover the initial topological wavefront in the far field (see Figure 6b). However, the resultant efficiency is relatively low, as most of the energy goes to the side lobes. Such a low-contrast subwavelength vortex beam becomes uncompetitive in terms of various applicable fields. By contrast, the sharp-edge diffraction of the randomly modulated structure considerably reduces the background field and enhance the contrast, as shown in Figure 6d–f. In this case, we obtain an obvious increase of the generation efficiency while maintaining the subwavelength feature size, as indicated in Figure 6f. Even though the sharp-edge aperture is randomly perturbed, the far-field light field exhibits well-defined helical wavefront (see Figure 6e), identical to that obtained from the circular aperture.

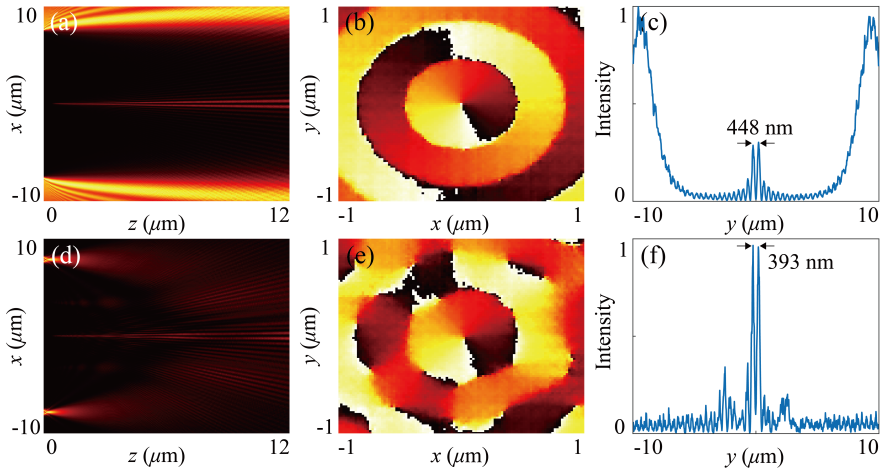


Figure 6. (**a**–**c**) Generation of the subwavelength nondiffracting vortex beams using a single circular sharp-edge aperture (without random modulation). (**a**) The recorded intensity distribution in the x-z plane. (**b**) The phase distribution in the transverse plane, recorded at the propagation distance of $z = 9$ μm. (**c**) One-dimensional intensity profiles recorded at the propagation distance of $z = 9$ μm reveal the subwavelength vortex field with peak-to-peak size measured as 448 nm. (**d**–**f**) Corresponding results obtained by using the six-fold ($n = 6$) petal-like sharp-edge aperture, which is randomly modulated with randomness strength set as $\varepsilon = 1$.

4. Conclusions

In summary, we numerically demonstrate a new mechanism for generating the high-contrast subwavelength nondiffracting structured light. Our working principle is mainly dependent on a randomized petal-like sharp-edge aperture. Specifically, by introducing randomized slit motifs into the circular obstacle, we are able to considerably reduce the background field by means of the random-induced destructive interference among the zero-order diffractive components while maintaining the constructive interference among the high-spatial-frequency diffractive components along the on-axis propagation positions. Our simulations show that we can increase the contrast from a relatively low value (η = ∼0.65) obtained from structure without the random modulation to a high value (η = ∼1.95) resulting from the randomly modulated structure. The proposed approach demonstrates strong robustness against the random perturbations and universality of the underlying mechanism. In addition to the realization of the zero-order Bessel-like beam

in the subwavelength scale, the proposed randomly modulated sharp-edge aperture allows to generate the higher-order Bessel-like vortex beam with feature size down to the subwavelength scale, which remains a challenge since the higher-order structured light with topological wavefront exhibits serious diffraction, particularly for those in the subwavelength scale [42]. These numerical results can be realized in experiments by using the advanced nano-fabrication techniques [36,37]. Our demonstration provides valuable guidelines for developing structured light field in the nano-scale regime, benefiting advanced applications such as in high-resolution microscopy [21], precision detection [43,44]. Moreover, the interaction between such highly localized light fields and matter could potentially trigger remarkable nonlinear effects [45–47], thereby further broadening applications.

Author Contributions: Conceptualization, S.F.; methodology, G.G., J.J., Y.H. and J.C.; software, G.G., J.J. and J.C.; investigation, G.G., J.J., X.Z., S.M., W.W. and H.L.; formal analysis, G.G., J.J., X.Z., S.M., W.W. and H.L.; data curation, G.G. and J.J.; resources, Y.H., Z.L. and S.F.; writing—original draft preparation, G.G. and J.J.; writing—review and editing, Y.H. and S.F.; visualization, G.G. and J.J.; supervision, Z.L., Y.H. and S.F.; project administration, Y.H., Z.L. and S.F. All authors have read and agreed to the published version of the manuscript.

Funding: This work was supported by the National Natural Science Foundation of China (Grants No. 12304358, No. 12374306, No. 12574355 and No. 12504382), the Guangzhou Science and Technology Project (Project No. SL2024A04J00688), the GuangDong Basic and Applied Basic Research Foundation (2025A1515011694), National Innovation and Entrepreneurship Training Program For Undergraduate (No. 202410559007), Innovation and Entrepreneurship Training Program For Undergraduate of Guangdong Province (No. S202410559092).

Institutional Review Board Statement: Not applicable.

Informed Consent Statement: Not applicable.

Data Availability Statement: Data underlying the results presented in this paper are not publicly available at this time but may be obtained from the authors upon reasonable request.

Conflicts of Interest: The authors declare no conflicts of interest.

References

1. Fu, S.; Tsur, Y.; Zhou, J.; Shemer, L.; Arie, A. Propagation Dynamics of Nonspreading Cosine-Gauss Water-Wave Pulses. *Phys. Rev. Lett.* **2015**, *115*, 254501. [CrossRef]
2. Minardi, S.; Eilenberger, F.; Kartashov, Y.V.; Szameit, A.; Röpke, U.; Kobelke, J.; Schuster, K.; Bartelt, H.; Nolte, S.; Torner, L.; et al. Three-Dimensional Light Bullets in Arrays of Waveguides. *Phys. Rev. Lett.* **2010**, *105*, 263901. [CrossRef]
3. Kurizki, G.; Kozhekin, A.E.; Opatrný, T.; Malomed, B.A. Optical solitons in periodic media with resonant and off-resonant nonlinearities. *Prog. Opt.* **2001**, *42*, 93–146.
4. Soa, S.; Kima, M.; Leea, D.; Nguyena, D.M.; Rho, J. Overcoming diffraction limit: From microscopy to nanoscopy. *Appl. Spectrosc. Rev.* **2018**, *53*, 290–312. [CrossRef]
5. Born, M.; Wolf, E. *Principles of Optics: Electromagnetic Theory of Propagation, Interference and Diffraction of Light*, 7th ed.; Cambridge University Press: Cambridge, MA, USA, 1999.
6. Durnin, J. Exact solutions for nondiffracting beams. I. The scalar theory. *J. Opt. Soc. Am. A* **1987**, *4*, 651–654. [CrossRef]
7. Durnin, J.; Miceli, J.J.; Eberly, J.H. Diffraction-free beams. *Phys. Rev. Lett.* **1987**, *58*, 1499–1501. [CrossRef]
8. Kartashov, Y.V.; Malomed, B.A.; Torner, L. Solitons in nonlinear lattices. *Rev. Mod. Phys.* **2011**, *83*, 405. [CrossRef]
9. Fu, S.; Zhou, J.; Li, Y.; Shemer, L.; Arie, A. Dispersion Management of Propagating Waveguide Modes on the Water Surface. *Phys. Rev. Lett.* **2018**, *118*, 144501. [CrossRef]
10. Malomed, B.A.; Mihalache, D.; Wise, F.; Torner, L. Spatiotemporal optical solitons. *J. Opt. B* **2005**, *7*, R53. [CrossRef]
11. Siviloglou, G.A.; Broky, J.; Dogariu, A.; Christodoulides, D.N. Observation of Accelerating Airy Beams. *Phys. Rev. Lett.* **2007**, *99*, 213901. [CrossRef]
12. Libster-Hershko, A.; Epstein, I.; Arie, A. Rapidly accelerating Mathieu and Weber surface plasmon beams. *Phys. Rev. Lett.* **2014**, *113*, 123902. [CrossRef]

13. Zhang, P.; Hu, Y.; Li, T.; Cannan, D.; Yin, X.; Morandotti, R.; Chen, Z.; Zhang, X. Nonparaxial Mathieu and Weber accelerating beams. *Phys. Rev. Lett.* **2012**, *109*, 193901. [CrossRef]
14. Efremidis, N.K.; Chen, Z.; Segev, M.; Christodoulides, D.N. Airy beams and accelerating waves: An overview of recent advances. *Optica* **2019**, *6*, 686–701. [CrossRef]
15. Lin, J.; Dellinger, J.; Genevet, P.; Cluzel, B.; de Fornel, F.; Capasso, F. Cosine-Gauss plasmon beam: A localized long-range nondiffracting surface wave. *Phys. Rev. Lett.* **2012**, *109*, 093904. [CrossRef] [PubMed]
16. Lin, Z.; Guo, X.; Tu, J.; Ma, Q.; Wu, J.; Zhang, D. Acoustic non-diffracting Airy beam. *J. Appl. Phys.* **2015**, *117*, 104503. [CrossRef]
17. Fu, S.; Tsur, Y.; Zhou, J.; Shemer, L.; Arie, A. Self-similar propagation of Hermite-Gauss water-wave pulses. *Phys. Rev. E* **2016**, *93*, 013127. [CrossRef]
18. Fu, S.; Tsur, Y.; Zhou, J.; Shemer, L.; Arie, A. Propagation dynamics of Airy water-wave pulses. *Phys. Rev. Lett.* **2015**, *115*, 034501. [CrossRef]
19. Voloch-Bloch, N.; Lereah, Y.; Lilach, Y.; Gover, A.; Arie, A. Generation of electron Airy beams. *Nature* **2013**, *494*, 331–335. [CrossRef]
20. Woerdemann, M.; Alpmann, C.; Esseling, M.; Denz, C. Advanced optical trapping by complex beam shaping. *Laser Photonics Rev.* **2013**, *7*, 839–854. [CrossRef]
21. Jia, S.; Vaughan, J.C.; Zhuang, X. Isotropic three-dimensional super-resolution imaging with a self-bending point spread function. *Nat. Photonics* **2014**, *8*, 302–306. [CrossRef] [PubMed]
22. Polynkin, P.; Kolesik, M.; Moloney, J.V.; Siviloglou, G.A.; Christodoulides, D.N. Curved plasma channel generation using ultraintense Airy beams. *Science* **2009**, *324*, 229–232. [CrossRef]
23. Fan, X.; Gensch, T.; Büldt, G.; Zhang, Y.; Musha, Z.; Zhang, W.; Roncarati, R.; Huang, R. Three dimensional drift control at nano-scale in single molecule localization microscopy. *Opt. Express* **2020**, *28*, 32750–32763. [CrossRef]
24. Zhou, Z.; Xing, Z.; Wang, Q.; Liu, J. Electrochemical Oxidation to Fabricate Micro-Nano-Scale Surface Wrinkling of Liquid Metals. *Small* **2023**, *19*, 2207327. [CrossRef] [PubMed]
25. Shah, M.; Wu, Y.; Chen, S.; Mead, J.L.; Hou, L.; Liu, K.; Tao, S.; Fatikow, S.; Wang, S. Recent advances in controlled manipulation of micro/nano particles: A review. *J. Phys. D Appl. Phys.* **2025**, *58*, 083001. [CrossRef]
26. Burresi, M.; Kampfrath, T.; van Oosten, D.; Prangsma, J.C.; Song, B.S.; Noda, S.; Kuipers, L. Magnetic Light-Matter Interactions in a Photonic Crystal Nanocavity. *Phys. Rev. Lett.* **2010**, *105*, 123901. [CrossRef] [PubMed]
27. Gramotnev, D.K.; Bozhevolnyi, S.I. Plasmonics beyond the diffraction limit. *Nat. Photonics* **2010**, *4*, 83–91. [CrossRef]
28. Zhan, Q. Evanescent Bessel beam generation via surface plasmon resonance excitation by a radially polarized beam. *Opt. Lett.* **2006**, *31*, 1726–1728. [CrossRef]
29. Chen, W.; Zhan, Q. Realization of an evanescent Bessel beam via surface plasmon interference excited by a radially polarized beam. *Opt. Lett.* **2009**, *34*, 722–724. [CrossRef]
30. Chen, J.; Hu, Y.; Yin, H.; Li, Z.; Chen, Z.; Fu, S. Theoretical study of freely propagating high-spatial-frequency optical waves. *Opt. Express* **2022**, *30*, 39510–39519. [CrossRef]
31. Hu, Y.; Wang, S.; Jia, J.; Fu, S.; Yin, H.; Li, Z.; Chen, Z. Optical superoscillatory waves without side lobes along a symmetric cut. *Adv. Photon.* **2021**, *3*, 045002. [CrossRef]
32. Hu, Y.; Fu, S.; Yin, H.; Li, Z.; Li, Z.; Chen, Z. Subwavelength generation of nondiffracting structured light beams. *Optica* **2020**, *7*, 1261–1266. [CrossRef]
33. Berry, M.V.; Popescu, S. Evolution of quantum superoscillations and optical superresolution without evanescent waves. *J. Phys. A Math. Gen.* **2006**, *39*, 6965–6977. [CrossRef]
34. Chen, G.; Wen, Z.Q.; Qiu, C.W. Superoscillation: From physics to optical applications. *Light Sci. Appl.* **2019**, *8*, 56. [CrossRef]
35. Lin, H.; Fu, S.; Deng, Z.; Zhou, H.; Yin, H.; Li, Z.; Chen, Z. Generation and Propagation of Optical Superoscillatory Vortex Arrays. *Ann. Phys.* **2019**, *531*, 1900240. [CrossRef]
36. Li, Y.; Shang, Z.; Li, Z.; Wu, S.; Dang, S.; Xia, L.; Zhou, Y.; Wen, Z.; Zhang, Z.; Xiang, J.; et al. Water-immersion metalens for generating superoscillation non-diffracting beams. *Opt. Laser Technol.* **2025**, *184*, 112492. [CrossRef]
37. Wen, J.; Chen, L.; Chen, X.; Kanwal, S.; Zhang, L.; Zhuang, S.; Zhang, D.; Lei, D. Use of dielectric metasurfaces to generate deep-subwavelength nondiffractive Bessel-like beams with arbitrary trajectories and ultralarge deflection. *Laser Photonics Rev.* **2021**, *15*, 2000487. [CrossRef]
38. Wu, Z.; Zhang, K.; Zhang, S.; Jin, Q.; Wen, Z.; Wang, L.; Dai, L.; Zhang, Z.; Chen, H.; Liang, G.; et al. Optimization-free approach for generating sub-diffraction quasi-non-diffracting beams. *Opt. Express* **2018**, *26*, 16585–16599. [CrossRef]
39. Cao, R.; Zhao, J.; Li, L.; Du, L.; Zhang, Y.; Luo, Y.; Jiang, L.; Davis, S.; Zhou, Q.; de la Zerda, A.; et al. Optical-resolution photoacoustic microscopy with a needle-shaped beam. *Nat. Photonics* **2012**, *17*, 89–95. [CrossRef] [PubMed]
40. Zheludev, N.I.; Yuan, G. Optical superoscillation technologies beyond the diffraction limit. *Nat. Rev. Phys.* **2022**, *4*, 16–32. [CrossRef]
41. Emile, O.; Emile, J. The Arago–Poisson Spot: New Applications for an Old Concept. *Photonics* **2024**, *11*, 55. [CrossRef]

42. Shen, Y.; Wang, X.; Xie, Z.; Min, C.; Fu, X.; Liu, Q.; Gong, M.; Yuan, X. Optical vortices 30 years on: OAM manipulation from topological charge to multiple singularities. *Light Sci. Appl.* **2019**, *8*, 90. [CrossRef] [PubMed]
43. Zhang, X.; Hu, Y.; Zhou, S.; Zeng, Z.; Liu, G.; Lin, H.; Li, Z.; Chen, Z.; Fu, S. Precise detection of tiny birefringence with accuracy reaching 10^{-11} level. *Nat. Commun.* **2025**, *16*, 6434. [CrossRef]
44. Yuan, G.; Zheludev, N.I. Detecting nanometric displacements with optical ruler metrology. *Science* **2019**, *364*, 771–775. [CrossRef]
45. Zhang, G.; Ma, L.; Lin, E.; Wang, Z.; Pan, J.; Yang, J.; Deng, M.; Wei, Y.; Ye, Y.; Wang, N.; et al. Periodically-modulated unipolar and bipolar orders in nematic fluids towards miniaturized nonlinear vectorial optics. *Nat. Commun.* **2025**, *16*, 9419. [CrossRef] [PubMed]
46. Zhang, S. Dynamically reprogrammable nonlinear Pancharatnam-Berry phase via ferroelectric nematic liquid crystals: A new paradigm for reconfigurable nonlinear optics. *Light Sci. Appl.* **2026**, *15*, 30. [CrossRef]
47. Liu, Y.; Zhou, L.; Neyts, K.; Sun, J.; Zhou, J. Second order optical nonlinearity originated from ferroelectric spherulite with vortex domain. *Adv. Opt. Mater.* **2025**, *13*, 2403095. [CrossRef]

Disclaimer/Publisher's Note: The statements, opinions and data contained in all publications are solely those of the individual author(s) and contributor(s) and not of MDPI and/or the editor(s). MDPI and/or the editor(s) disclaim responsibility for any injury to people or property resulting from any ideas, methods, instructions or products referred to in the content.